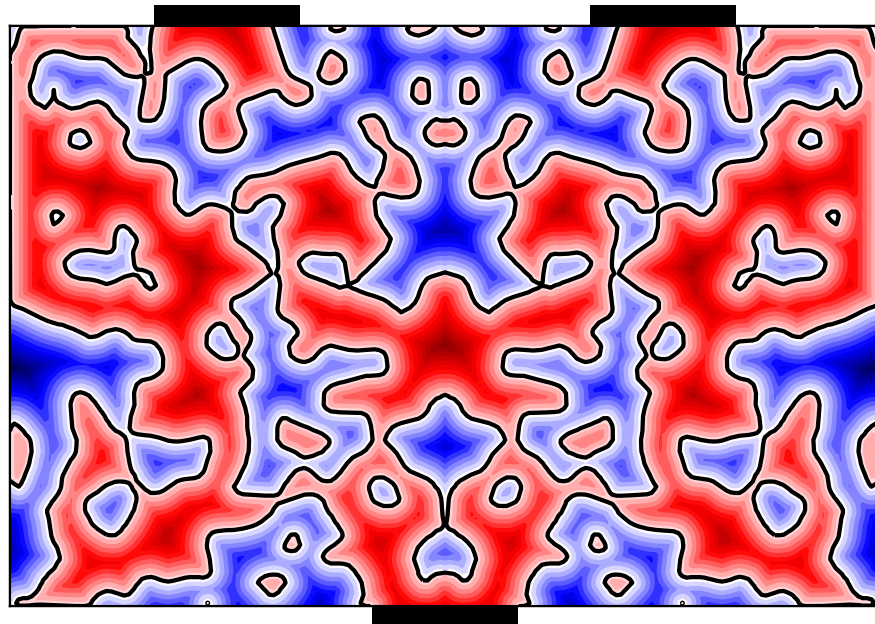




CHALMERS
UNIVERSITY OF TECHNOLOGY



Inverse Design of Traveling-Wave Phononic Devices

Master's thesis in Physics

DAVID HAMBRAEUS

DEPARTMENT OF MICROTECHNOLOGY AND NANOSCIENCE

CHALMERS UNIVERSITY OF TECHNOLOGY

Gothenburg, Sweden 2023

www.chalmers.se

MASTER'S THESIS 2023

Inverse Design of Traveling-Wave Phononic Devices

David Hambraeus



CHALMERS
UNIVERSITY OF TECHNOLOGY

Department of Microtechnology and Nanoscience
Quantum Technology Laboratory
Quantum Photonics Laboratory
CHALMERS UNIVERSITY OF TECHNOLOGY
Gothenburg, Sweden 2023

Inverse Design of Traveling-Wave Phononic Devices
David Hambraeus

© David Hambraeus, 2023.

Supervisor: Raphaël van Laer, QPL
Examiner: Raphaël van Laer, QPL

Master's Thesis 2023
Department of Microtechnology and Nanoscience
Quantum Technology Laboratory
Quantum Photonics Laboratory
Chalmers University of Technology
SE-412 96 Gothenburg
Telephone: +46 31 772 1000

Cover: Signed distance field of optimized level-set beamsplitter design.

Typeset in L^AT_EX
Printed by Chalmers Digital Printing
Gothenburg, Sweden 2023

Inverse Design of Traveling-Wave Phononic Devices:

David Hambraeus
Department of Microtechnology and Nanoscience
Chalmers University of Technology

Abstract

Phononic devices could enable and improve a broad range of functions in the realm of classical and quantum information processing. However, such devices are currently often designed by hand, combined with brute force parameter sweeps, which severely limits the designs that can be investigated. This work presents a method for inverse-design of phononic devices, allowing a vastly larger design space to be explored. At the heart of the method lies a fast calculation of gradients using the adjoint method, whereby the gradient computation costs no more than a single normal simulation. I show that this method is theoretically applicable to phononic devices, and demonstrate that it works in simulation. As a proof of concept, I attempt to design a phononic beamsplitter. The design process consists of two steps: one with continuously varying materials which is non-physical, but easier to optimize; and one with binary devices, accomplished through level-set methods. The first step yielded near perfect performance, achieving less than one percent reflection and almost nothing being scattered into other modes. The second step never reached quite as good performance, though still a 45/45 split was obtained with less than 10 % of the power reflected. With some tweaking of the second step, this method looks promising for use in the design of future phononic devices.

Keywords: phononic devices, quantum acoustics, inverse design, adjoint method, level-set, gradient descent, solid mechanics.

Acknowledgements

 Lorem ipsum dolor sit amet, consectetur adipisicing elit, sed do eiusmod tempor incididunt ut labore et dolore magna aliqua. Ut enim ad minim veniam, quis nostrud exercitation ullamco laboris nisi ut aliquip ex ea commodo consequat. Duis aute irure dolor in reprehenderit in voluptate velit esse cillum dolore eu fugiat nulla pariatur. Excepteur sint occaecat cupidatat non proident, sunt in culpa qui officia deserunt mollit anim id est laborum.

 David Hambraeus, Gothenburg, June 2023

Table of contents

List of figures	ix
List of tables	xi
Acronyms	xiii
1 Introduction	1
1.1 Aim and Thesis Outline	2
2 Acoustic Waves and Waveguides	5
2.1 The Frequency Domain Acoustic Equation	5
2.2 Bloch States and Band Diagrams	6
2.2.1 Concrete Example of a Phononic Crystal	7
3 Inverse Design	11
3.1 Adjoint Simulation	11
3.1.1 General Derivation	11
3.1.2 Specific Derivation with Acoustics	12
3.2 Optimization Algorithms	16
3.2.1 Gradient Descent	16
3.2.2 Adaptive Moment Estimation (ADAM)	17
4 Methods	21
4.1 Design	21
4.1.1 Objective Function	21
4.1.2 Excitation	23
4.1.3 Perfectly Matched Layers (PMLs)	23
4.1.4 Level-Set	25
4.2 Optimization	27
4.3 Simulations	28
5 Results and Discussion	31
5.1 Long Waveguide Simulations	31
5.1.1 Excitation	31
5.1.2 PML Investigation	32
5.2 Continuous Optimization	32
5.3 Level-Set Optimization	36
6 Concluding Remarks	39
6.1 Future Research	39

Table of contents

References	41
-------------------	-----------

List of figures

2.1	Top down view of unit cell of a phononic crystal. The periodicity of the waveguide is a , the width is w and h_x and h_y are the major and minor radii of the elliptic hole.	7
2.2	Band diagram of phononic crystal defined in figure 2.1.	8
2.3	Mode shapes for the lowest eight modes at $k = 0.9\pi/a$. The color denotes the absolute value of the displacement, and the scale is normalized for each figure.	9
3.1	A comparison between Adaptive Moment Estimation (ADAM) and Gradient Descent (GD) in an optimization landscape with a narrow canyon. The two different GD algorithms are shown with 1000 steps, while 200 steps with the ADAM algorithm are shown.	18
4.1	Device design to be optimized. At the red line, a wave traveling right is excited. The output is measured over the blue unit cells. The dashed unit cells are Perfectly Matched Layers (PMLs). The large, rectangular design area has dimensions $d_x \times d_y \times h$	22
4.2	This figure shows the effect of changing different parameters. The green curves shows changing d while keeping the other parameters fixed, and the orange and blue show s and n respectively. Darker colour means higher value, and the last green curve coincides with the first orange, and the last orange with the first blue.	24
4.3	For the green curve, the initial sudden increase of the imaginary component of the density at the beginning of the PML causes reflections. For the blue curve, the beginning of the PML is smooth but there is an increase partway through sharp enough to cause reflections. For the orange curve, the PML never becomes strong enough to completely dampen the waves, and they get reflected at the end.	25
4.4	Possible evolution of boundary. In the leftmost figure, the boundary is defined by pretty much evenly spaced points. In the center figure the boundaries have moved and the spacing is no longer even, and the right circle is very poorly resolved. The rightmost figure shows the boundary after the two circles moved closer together. Now there are multiple points that need to be removed, marked in red, and the connectivity of the points that remain must be changed such that the two boundaries are merged.	26
4.5	Example of three signed distance functions for three different boundaries.	26
4.6	Adding s to the signed distance function shifts boundary by s	27

5.1	This figure shows the long waveguide used for the PML simulations as wells as validating the excitation method.	31
5.2	Fourier transform of the y-component of the displacement field. It clearly shows one wave traveling forward with a k-vector of $0.9\pi/a$, where the dashed gray line is. Since the closest other mode at this frequency is at $k_y \approx 0.4\pi/a$, where no peak is visible, it is concluded that solely the desired mode is excited.	32
5.3	33
5.4	Non-converging optimization example. The blue curve shows the transmitted power in one of the output arms as a function of iteration, while the yellow shows the power reflected back out through the input. The cases where two times the blue plus the yellow isn't 1.0 is explained by power exiting through a different mode.	34
5.5	This figure shows a quadratic spline approximation to a sine function, given eight points on the function. Even though the spline approximates the sine function very well, the second derivative approximation is terrible.	35
5.6	Similar to figure 5.4, but at iteration 467 and 615, a sigmoid function was abruptly applied to the design field, which causes the dips. The final device was a near perfect beamsplitter, with less than 1 % of the power begin reflected, and nothing being scattered into other modes.	35
5.7	This figure shows the interpolation field at iteration 467, 615, and 830. It is clearly seen that the device becomes closer and closer to being binary.	36
5.8	Performance evolution of the level-set device during optimization. The curve is not as smooth as the curve from the continuous optimization, which indicates that the step size is closer to being too large.	36
5.9	This figure shows the final optimized design for the level-set optimization. The device performs a roughly 45/45 split of the incoming power, with the rest of the power being reflected.	37

List of tables

4.1 Values for the geometric parameters of the device. Reference figures 2.1 and 4.1 for what the quantities mean.	22
---	----

List of tables

Acronyms

ADAM Adaptive Moment Estimation. ix, 16–18, 27

GD Gradient Descent. ix, 17, 18

PML Perfectly Matched Layer. ix, x, 22–25, 31–33

Acronyms

1. Introduction

In recent years, the research into quantum devices of different kinds has significantly intensified. Much of it is in one way or another connected to the construction or operation of a quantum computer. Though many people are focusing on superconducting circuits, where quanta of microwave-frequency light are manipulated, there has also been a growing interest in a different medium for quantum information: sound. More precisely, acoustic waves in solid materials. Just like how light, or electromagnetic waves, come in quantized packets of energy called photons, so too does acoustic waves and those packets are called phonons. Just recently, in 2019, researchers coupled an acoustic resonator to a transmon qubit and were able to directly measure the presence or absence of single phonons [1].

Possible applications of quantum acoustic devices, also called phononic devices, are many. One of them is quantum memory [2]. Regular computers have both memory and a processing unit that retrieves data from memory, applies operations on it, and then returns it to memory. Keeping all of the data inside the processing unit would be very inefficient, since the processing unit would then have to be very large. The same goes for quantum computers: storing all of the quantum information in the same place where the computation happens is not scalable. Instead, a quantum memory could be used to store information while it is not directly needed for the computation. The reason for using mechanical resonators is that they have been shown to achieve very long lifetimes [3]. Another application of quantum acoustics worth mentioning is coherent transduction between microwave and optical photons. This would enable communication between physically separated superconducting circuit based quantum computers [4]. A third possible application is doing quantum information processing purely in mechanical elements [5].

One important problem with such quantum acoustic devices is that they can be hard to design. Currently they are often designed by hand, through analytical derivations or analytically motivated guesswork, combined with brute force parameter sweeps. However, this severely limits the designs that can be investigated: sometimes analytical derivations are impossible, and brute force parameter sweeps quickly become computationally intractable. A parameter sweep of just 6 parameters with 10 different values for each requires 1 000 000 simulations. One can of course use smarter optimization algorithms like bayesian optimization or particle swarm optimization [6], [7] to decrease the number of simulations needed, but it will still be of the same approximate order.

A different approach that has been gaining some popularity in the field of nanophotonics is *inverse design with adjoint simulation* [8]. The idea is that if the

gradient of the figure of merit with respect to the parameters can be calculated, then gradient based optimization methods can be used. These converge much faster, even if the number of parameters is very large. Thus, one hopes to be able to search among a much more general class of designs for the optimal one. This has been successfully applied to photonic devices, where a wide variety of components have been designed [9]. In some cases, for example the waveguide bend, the inverse-designed device could be made much more compact than conventionally designed bends [10]. In other cases, for example the vertically-incident wavelength-demultiplexing grating coupler, there are no other known conventional methods of designing the device [11]. However, to our knowledge, no one has yet applied this method to phononic devices, though there is some work on another type of inverse design of phononics using machine learning models [12].

Phononic devices have in general been studied less than photonic devices, and the library of known devices is very small. With this thesis, I explore the possibility of extending the inverse-design paradigm to quantum acoustic devices. Since both acoustics and electromagnetics are wave phenomena, there are many analogies to be drawn, but there are also important differences. I have in this work shown that the adjoint method is applicable to the case of acoustics, as well as derived the form of the equations. As a proof of concept, I attempt to design a phononic 50/50 beamsplitter. The beamsplitter is conceptually one of the simplest devices imaginable, and photonic beamsplitters have been studied in great detail for many years and found a multitude of uses in many different experiments. However, there is still no standard implementation for phononic beamsplitters, though [5] has demonstrated a working beamsplitter for surface acoustic waves. There are two major differences between their design and the one attempted here. Firstly, they are using surface acoustic waves while I am using wave propagating through patterned silicon waveguides. Secondly, their beamsplitter reflects one of the arms of the beamsplitter back towards the source, whereas I have one input waveguide and two separate outputs.

1.1 Aim and Thesis Outline

The aims of this thesis are:

- Rederive the equations for inverse design with adjoint simulation in the case of acoustics and confirm that the methods are theoretically applicable.
- Implement the methods and use them to design a phononic beamsplitter.

Chapter 2 presents some of the theory on solid mechanics and acoustic waves needed to understand the thesis. A band diagram over the modes of the waveguide used is also shown there. In chapter 3, the inverse design process is presented. First, the general adjoint method is showcased, followed by a derivation in the specific case of acoustics. Then, gradient based optimization algorithms are discussed and the ones used in this thesis are presented. Chapter 4 describes the specifics of the simulations performed in this work: both a specification of the skeleton of the devices, how the

input wave was excited, and how the designs were parametrized. It also describes the specifics of the optimization algorithm, including parameter values. Chapter 5 then presents and analyzes the results of the simulations performed and Chapter 6 summarizes the conclusions drawn from the results and describes possible future research.

1. Introduction

2. Acoustic Waves and Waveguides

In this chapter, the theory of the physics behind my simulations is given. Section 2.1 gives a review of solid mechanics in the frequency domain, culminating in equation (2.13), which is the equation that is solved each simulation. Section 2.2 goes on to show that the solutions to this equation with no external forces for infinite periodic structures can be obtained from simulating a single unit cell of the structure. Lastly, the solutions for the specific periodic structure used for the inputs and outputs in this thesis are shown with a band diagram as well as the shapes of the modes.

2.1 The Frequency Domain Acoustic Equation

In order to efficiently model the deformation and stresses in a solid material, a linear elasticity model is often assumed. This means the force is assumed to be linear with displacement, which is a valid approximation for small displacements. The basic equation is Hooke's law, $F = kx$ for ideal springs, that everybody learns in their first mechanics course. Since we are dealing with solid elements in three dimensions rather than ideal springs in one dimension, the equation changes slightly but the essence is still the same. Hooke's law in its full form is

$$\sigma = C : \epsilon \quad (2.1)$$

where σ is the stress tensor, C the elasticity tensor, a rank four tensor that is a property of the material,

$$\epsilon := \frac{1}{2}(\nabla \mathbf{u} + (\nabla \mathbf{u})^\top) \quad (2.2)$$

is the strain tensor, and $:$ denotes double scalar product¹. Equation (2.1) is linear in \mathbf{u} , hence the name *linear* elasticity. Using this and Newton's equations of motion, the equation governing the dynamics is obtained:

$$\rho \ddot{\mathbf{u}} = \nabla \cdot \sigma + \mathbf{F}, \quad (2.3)$$

where ρ is the density, \mathbf{u} is the displacement and \mathbf{F} is the externally applied force. If the force is sinusoidally varying with some frequency ω , $\mathbf{F}(\mathbf{x}, t) = \mathbf{F}(\mathbf{x})e^{i\omega t}$, then \mathbf{u} is also expected to be oscillating with that same frequency: $\mathbf{u}(\mathbf{x}, t) = \mathbf{u}(\mathbf{x})e^{i\omega t}$. Inserting this in equation (2.3) gives

$$-\rho\omega^2 \mathbf{u} = \nabla \cdot \sigma + \mathbf{F}. \quad (2.4)$$

¹See equation (2.6) for what the double scalar product means in this case. It is in general a product that contracts two indices, as opposed to the regular scalar product that contracts only one.

To combine equations (2.1) to (2.4) into one equation that can be solved for \mathbf{u} , we first rewrite them in index notation to make calculations clearer. Note that throughout this thesis, the Einstein summation convention is used, meaning that repeated indices are summed.

$$\epsilon_{ij} = \frac{1}{2}(\partial_i u_j + \partial_j u_i) \quad (2.5)$$

$$\sigma_{ij} = C_{ijkl}\epsilon_{kl} \quad (2.6)$$

$$= \frac{1}{2} (C_{ijkl}\partial_k u_l + C_{ijkl}\partial_l u_k) \quad (2.7)$$

$$= C_{ijkl}\partial_k u_l \text{ because of the symmetry } C_{ijkl} = C_{ijlk} \quad (2.8)$$

which gives

$$F_i = -\rho\omega^2 u_i - \partial_j \sigma_{ij} \quad (2.9)$$

$$= -\rho\omega^2 \delta_{ik} u_k - \partial_j (C_{ijkl}\partial_l u_k) \quad (2.10)$$

$$= -\left(\rho\omega^2 \delta_{ik} \cdot + \partial_j (C_{ijkl}\partial_l \cdot)\right) u_k \quad (2.11)$$

where the indices i, j, k, l go over the spatial dimensions x, y, z . All of the tensors in the equation above are really tensor fields, i.e. they are functions of \mathbf{x} . Defining the operator

$$\hat{A}_{ik} = -\left(\rho\omega^2 \delta_{ik} \cdot + \partial_j (C_{ijkl}\partial_l \cdot)\right) \quad (2.12)$$

we can write

$$\hat{A}_{ik} u_k = F_i. \quad (2.13)$$

Solving this equation for \mathbf{u} thus gives the response of the system to periodically varying force $\mathbf{F}(\mathbf{x}, t) = \mathbf{F}(\mathbf{x})e^{i\omega t}$.

2.2 Bloch States and Band Diagrams

With no external forces, i.e. $F_i = 0$, equation (2.13) can be written as

$$\frac{1}{\rho} \partial_j (C_{ijkl}\partial_l u_k) = \omega^2 u_i, \quad (2.14)$$

which is an eigenvalue equation for the operator $\hat{O}_{ik} = \frac{1}{\rho} \partial_j (C_{ijkl}\partial_l \cdot)$ where eigenvalues are the angular frequency squared. If furthermore the structure is periodic, then the eigenstates are so called *Bloch states*.

If the structure is periodic in the y direction with some periodicity $\mathbf{a} = a\hat{\mathbf{y}}$, meaning that $C_{ijkl}(\mathbf{x}) = C_{ijkl}(\mathbf{x} + n\mathbf{a})$ and $\rho(\mathbf{x}) = \rho(\mathbf{x} + n\mathbf{a})$ where n is an integer, then this operator commutes with the translation operator $\hat{T}_a[\mathbf{u}(\mathbf{x})] = \mathbf{u}(\mathbf{x} + \mathbf{a})$. This means that there is a basis of simultaneous eigenstates of both operators. The eigenfunctions of the translation operator are $\mathbf{f}(x, z)e^{ik_y y}$, where \mathbf{f} is an arbitrary function, and the eigenvalues are $e^{ik_y a}$. Defining the reciprocal lattice constant $b = 2\pi/a$, we see that

the functions $\mathbf{f}(x, z)e^{i(k_y + mb)y}$ for integer values of m all have the same eigenvalue, which means that they form a degenerate subspace of eigenfunctions. This also means that we can restrict ourselves to the first Brillouin zone: $k_y \in [-b/2, b/2]$, since any k_y outside this interval can be written as $k'_y + mb$ with $k'_y \in [-b/2, b/2]$. Thus, the simultaneous eigenstate $\mathbf{u}_{k_y, \omega^2}$ can be written

$$\mathbf{u}_{k_y, \omega^2}(\mathbf{x}) = \sum_m \mathbf{f}_{m, k_y, \omega^2}(x, z) e^{i(k_y + mb)y} = e^{ik_y y} \tilde{\mathbf{f}}_{k_y, \omega^2}(\mathbf{x}) \quad (2.15)$$

where $\tilde{\mathbf{f}}_{k_y, \omega^2}$ is a periodic function with periodicity \mathbf{a} by construction [13].

The solutions to these eigenvalue equations are often called modes, and each mode has both a frequency and a wave vector. This gives rise to a band diagram, where the frequency is plotted as a function of the wave vector.

2.2.1 Concrete Example of a Phononic Crystal

In this work, a rectangular silicon waveguide patterned with elliptic holes is used. The structure is clamped at the bottom (meaning that a fixed boundary condition is used there, enforcing $\mathbf{u} = 0$) while the other sides are free. A top down schematic of the unit cell can be seen in figure 2.1. The reason for using this specific unit cell is that it has been shown to enable good coupling between optical and mechanical modes while still being clamped to a substrate, which improves thermal properties [14].

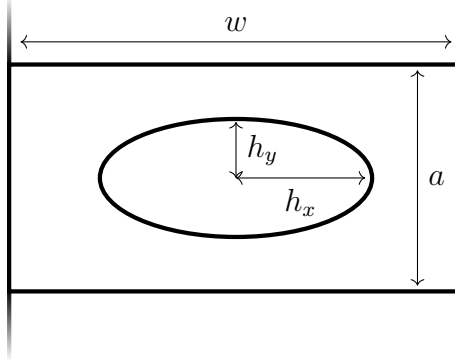


Figure 2.1: Top down view of unit cell of a phononic crystal. The periodicity of the waveguide is a , the width is w and h_x and h_y are the major and minor radii of the elliptic hole.

An infinite waveguide can be simulated with just one unit cell using periodic boundary conditions at the edge where the unit cell would be attached to the next one. As section 2.2 showed, waves with any \mathbf{k} can be investigated with a single unit cell since \mathbf{u} is a phase factor $e^{i\mathbf{k}\cdot\mathbf{x}}$ times some function with the same periodicity as the unit cell. Enforcing a wave vector $\mathbf{k} = k\hat{\mathbf{y}}$ thus entails using periodic boundary conditions with a specified phase shift over the unit cell. These are called *floquet periodic boundary conditions* in COMSOL, which is the simulation software used throughout this thesis. Running simulations with different k to find the eigenmodes with their corresponding frequencies for this structure yields the band diagram in

figure 2.2. The parameter values used in the simulations can be found in table 4.1. Figure 2.3 shows the shapes of the eight lowest lying eigenmodes at $k = 0.9\pi/a$.

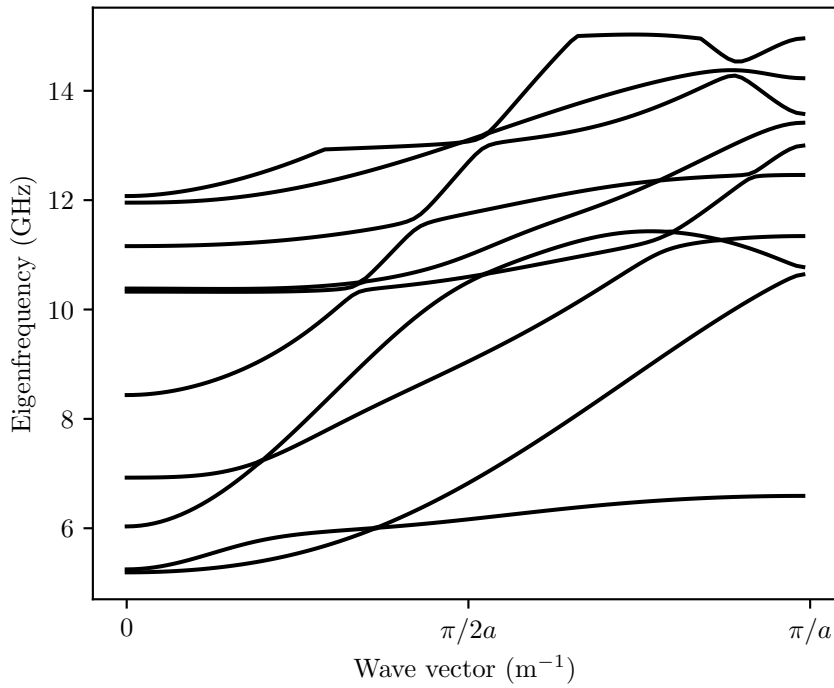


Figure 2.2: Band diagram of phononic crystal defined in figure 2.1.

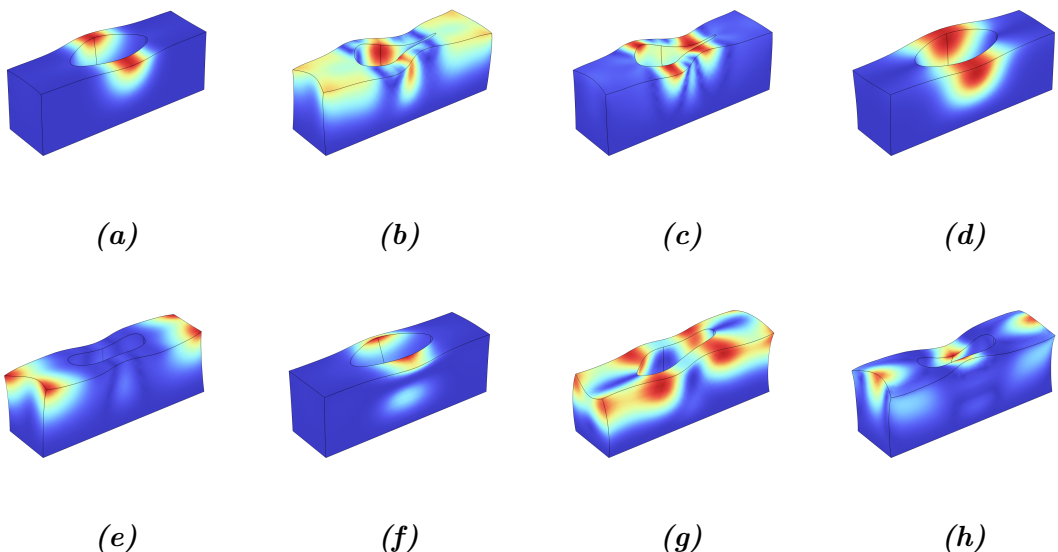


Figure 2.3: Mode shapes for the lowest eight modes at $k = 0.9\pi/a$. The color denotes the absolute value of the displacement, and the scale is normalized for each figure.

2. Acoustic Waves and Waveguides

3. Inverse Design

Inverse design is a design paradigm where the design of a device is guided fully by the desired characteristics. These desired characteristics are quantified through what is called an objective function², which we will denote f_{obj} , that should be maximized. When coupled with *adjoint simulation*, which is a clever way to compute gradients, and gradient based optimization algorithms this becomes a very powerful methodology.

An overview of the design process is as follows:

1. Initialize a random device design.
2. Calculate the gradient of the design through the adjoint method.
3. Update the device design using the gradient according to the optimization algorithm.
4. If the device performance is good enough, terminate optimization, else return to step 2.

3.1 Adjoint Simulation

Adjoint simulation is a way to compute the gradient of f_{obj} with respect to the design, which in our case means with respect to the material parameters. I will in this section first give a general derivation, following reference [15]. In section 3.1.2 I will then derive the specifics when applying this to acoustics.

3.1.1 General Derivation

Let f_{obj} be a function which depends on some high-dimensional vector v . The vector v can be calculated by solving the linear equation $Av = b$, where b is a fixed vector and A is a matrix that depends on a vector of design parameters p . This could be the acoustics equation, but it might also be the analogous equation for photonics, or something completely different like fluid dynamics. I will refer to the process of solving this equation as a simulation, since for this thesis it is solved through the simulation software COMSOL. The overall goal is to find the parameters p that maximize the objective function f_{obj} . The goal of adjoint simulation is to find $\frac{df_{\text{obj}}}{dp}$.

²Also called *figure of merit (FOM)*.

This can be expanded through the chain rule as

$$\frac{df_{\text{obj}}}{dp} = \frac{df_{\text{obj}}}{dv} \frac{dv}{dp}. \quad (3.1)$$

To find the latter factor we do

$$\frac{d}{dp}[Av = b] \implies \frac{dA}{dp}v + A\frac{dv}{dp} = 0 \quad (3.2)$$

$$\implies A\frac{dv}{dp} = -\frac{dA}{dp}v. \quad (3.3)$$

Thus, if we can find a \tilde{v} such that

$$\frac{df_{\text{obj}}}{dv} = \tilde{v}A \quad (3.4)$$

then

$$\frac{df_{\text{obj}}}{dp} = \tilde{v}A\frac{dv}{dp} \quad (3.5)$$

$$= -\tilde{v}\frac{dA}{dp}v. \quad (3.6)$$

Finding \tilde{v} from equation (3.4) amounts to solving the so called *adjoint problem*:

$$A^\dagger \tilde{v}^\dagger = \frac{df_{\text{obj}}}{dv}^\dagger \quad (3.7)$$

hence the name adjoint method. As it turns out, A is in many cases symmetric (or self-adjoint) which means that this is simply a normal simulation but with $df_{\text{obj}}/dv^\dagger$ as the source. Thus, to obtain the derivative we just need to run an additional simulation with a different input.

Now you might be wondering: what have we gained by this? Let n be the dimension of v , m the dimension of p and l the dimension of b . This means that A is a matrix with dimension $l \times n$ and dA/dp is a rank three tensor with dimension $m \times l \times n$. Thus solving for dv/dp from equation equation (3.3) means solving for an $n \times m$ matrix, which much more computationally expensive than solving for just a vector of dimension n .

3.1.2 Specific Derivation with Acoustics

Now we turn to the specific case of acoustic devices. Here $Av = b$ is replaced by the acoustic field equation (equation (2.13)):

$$\hat{A}_{ik}u_k = F_i. \quad (3.8)$$

Instead of vectors, like we saw in section 3.1.1, these quantities are now functions³ of \mathbf{x} . Analogously to the vector of design parameters we now have a *design field* $p(\mathbf{x})$, and analogously to f_{obj} being a function of a vector, this f_{obj} is a function of a function, i.e. a *functional*. For a quick overview of functionals and their derivatives, see box 3.1.

³Vector-valued functions, but that is not the important part here.

Box 3.1: On functionals and their derivatives

Our f_{obj} is no longer a function, but rather a *functional*, and thus we need to use the functional derivative instead of the ordinary derivative. One can think of a functional as a function of a function, i.e. something that maps an element of a function space to a scalar number. There are also functionals which depend on both a function and a real number, or on multiple functions. Below I will give an overview of the notational conventions I use, and then give the definition of the functional derivative as well as some useful properties of it.

Let \mathcal{Y} be a function space of functions $\mathbb{R} \rightarrow \mathbb{R}$. A functional $F : \mathcal{Y} \rightarrow \mathbb{R}$ evaluated at the function $f \in \mathcal{Y}$ is denoted with the function in square brackets: $F[f]$. Note that in principle, F is the functional while $F[f]$ is just a number, analogously to how f is a function while $f(x)$ is a real number. If the functional additionally depends on a real number, $G : \mathcal{Y} \times \mathbb{R} \rightarrow \mathbb{R}$, that is put in round brackets: $G[f](x)$.

The functional derivative of F with respect to its function argument is a functional $\mathcal{Y} \times \mathbb{R} \rightarrow \mathbb{R}$ denoted $\delta F[f]/\delta f$. In this expression, f is technically a dummy function, writing $\delta F[g]/\delta g$ is exactly the same functional. However, often the argument of F is omitted and the function in the denominator is named in accordance with the names in the definition of the functional. Furthermore, the same notation is also often used to denote the functional derivative evaluated at a certain function. For example, if we define a functional taking two function arguments $F[f_1, f_2] = \int f_1(x) + f_2(x) dx$, one can write

$$\frac{\delta F}{\delta f_2}(x) \quad \text{meaning} \quad \frac{\delta F[g_1, g_2]}{\delta g_2}(x) \quad (3.9)$$

$$\frac{\delta F}{\delta f_2}(x) \quad \text{meaning} \quad \frac{\delta F[g_1, g_2]}{\delta g_2}[f_1, f_2](x) \quad (3.10)$$

where in the latter case, f_1 and f_2 are specific functions defined previously. Also note that the scalar argument to the functional derivative can be put either in the denominator or after, depending on what is more convenient. Oftentimes, when the functional being differentiated is a long expression and is placed after the fraction, the argument is placed in the denominator:

$$\frac{\delta F}{\delta f}(x) = \frac{\delta F}{\delta f(x)} = \frac{\delta}{\delta f(x)} F \quad (3.11)$$

The functional derivative is defined by

$$\int \frac{\delta F}{\delta f}(x)\varphi(x) dx = \frac{d}{d\varepsilon} F[f + \varepsilon\varphi] \quad (3.12)$$

where F is a functional of f and φ is an arbitrary test function. We will use two properties of the functional derivative:

3. Inverse Design

- If F is the functional $F[f](y) = f(y)$, then $\delta F(y)/\delta f(x) = \delta(y - x)$.
- The chain rule: if F is a functional with one function argument, G is a functional with one function and one real argument, and H is the functional defined as $H[f] = F[G[f](y)]$, then

$$\frac{\delta H}{\delta f}(x) = \int \frac{\delta F}{\delta G[f]}(y) \frac{dG(y)}{df}(x) dy \quad (3.13)$$

For simplicity we will limit ourselves to the case where the objective function is an overlap integral of the displacement field $u_k(\mathbf{x})$ with some function $\varphi_k^*(\mathbf{x})$:

$$f_{\text{obj}}[\mathbf{u}] = \int_{\Omega} u_i(\mathbf{x}) \varphi_i^*(\mathbf{x}) d\mathbf{x}. \quad (3.14)$$

where Ω is the domain of \mathbf{u} . Such an integral is an inner product in the space of functions on Ω .

Analogously to the general derivation in section 3.1.1, the chain rule is used to expand $\delta f_{\text{obj}}/\delta p(\mathbf{x})$, see box 3.1 for the form of the chain rule for the functional derivative. However, because \mathbf{u} is in general complex, we will split it into its real and imaginary components: $\mathbf{u} = \mathbf{v} + i\mathbf{w}$.

$$\frac{\delta f_{\text{obj}}}{\delta p}(\mathbf{x}) = \int_{\Omega} d\mathbf{y} \frac{\delta f_{\text{obj}}}{\delta v_i}(\mathbf{y}) \frac{\delta v_i(\mathbf{y})}{\delta p}(\mathbf{x}) + \frac{\delta f_{\text{obj}}}{\delta w_i}(\mathbf{y}) \frac{\delta w_i(\mathbf{y})}{\delta p}(\mathbf{x}) \quad (3.15)$$

The first factor of each of the two terms is easy enough to calculate:

$$\frac{\delta f_{\text{obj}}}{\delta v_i}(\mathbf{y}) = \frac{\delta}{\delta v_i(\mathbf{y})} \int_{\Omega} u_j(\mathbf{x}) \varphi_j^*(\mathbf{x}) d\mathbf{x} \quad (3.16)$$

$$= \int_{\Omega} \frac{\delta}{\delta v_i(\mathbf{y})} u_j(\mathbf{x}) \varphi_j^*(\mathbf{x}) d\mathbf{x} \quad (3.17)$$

$$= \int_{\Omega} \delta(\mathbf{x} - \mathbf{y}) \delta_{ij} \varphi_j^*(\mathbf{x}) d\mathbf{x} \quad (3.18)$$

$$= \varphi_i^*(\mathbf{y}) \quad (3.19)$$

and

$$\frac{\delta f_{\text{obj}}}{\delta w_i}(\mathbf{y}) = \frac{\delta}{\delta w_i(\mathbf{y})} \int_{\Omega} u_j(\mathbf{x}) \varphi_j^*(\mathbf{x}) d\mathbf{x} \quad (3.20)$$

$$= \int_{\Omega} \frac{\delta}{\delta w_i(\mathbf{y})} u_j(\mathbf{x}) \varphi_j^*(\mathbf{x}) d\mathbf{x} \quad (3.21)$$

$$= \int_{\Omega} i \delta(\mathbf{x} - \mathbf{y}) \delta_{ij} \varphi_j^*(\mathbf{x}) d\mathbf{x} \quad (3.22)$$

$$= i \varphi_i^*(\mathbf{y}) \quad (3.23)$$

which gives us

$$\frac{\delta f_{\text{obj}}}{\delta p}(\mathbf{x}) = \int_{\Omega} d\mathbf{y} \varphi_i^*(\mathbf{y}) \frac{\delta v_i(\mathbf{y})}{\delta p}(\mathbf{x}) + i \varphi_i^*(\mathbf{y}) \frac{\delta w_i(\mathbf{y})}{\delta p}(\mathbf{x}) \quad (3.24)$$

$$= \int_{\Omega} d\mathbf{y} \varphi_i^*(\mathbf{y}) \operatorname{Re} \left(\frac{\delta u_i(\mathbf{y})}{\delta p}(\mathbf{x}) \right) + i \varphi_i^*(\mathbf{y}) \operatorname{Im} \left(\frac{\delta u_i(\mathbf{y})}{\delta p}(\mathbf{x}) \right) \quad (3.25)$$

$$= \int_{\Omega} d\mathbf{y} \varphi_i^*(\mathbf{y}) \frac{\delta u_i(\mathbf{y})}{\delta p}(\mathbf{x}) \quad (3.26)$$

To find $\delta u_i(\mathbf{y})/\delta p(\mathbf{x})$ we apply $\delta/\delta p(\mathbf{x})$ to equation (3.8), which gives us

$$0 = \frac{\delta \hat{A}_{ik}(\mathbf{y})}{\delta p}(\mathbf{x}) u_k(\mathbf{y}) + \hat{A}_{ik}(\mathbf{y}) \frac{\delta u_k(\mathbf{y})}{\delta p}(\mathbf{x}) \quad (3.27)$$

Just like equation (3.5), we want an adjoint field $\tilde{\mathbf{u}}$ such that the integral in equation (3.26) is

$$\int_{\Omega} d\mathbf{y} \varphi_i^*(\mathbf{y}) \frac{\delta u_i(\mathbf{y})}{\delta p}(\mathbf{x}) = \int_{\Omega} d\mathbf{y} \tilde{u}_i(\mathbf{y}) \hat{A}_{ik}(\mathbf{y}) \frac{\delta u_k(\mathbf{y})}{\delta p}(\mathbf{x}) \quad (3.28)$$

which by equation (3.27) is equal to

$$- \int_{\Omega} d\mathbf{y} \tilde{u}_i(\mathbf{y}) \frac{\delta \hat{A}_{ik}(\mathbf{y})}{\delta p}(\mathbf{x}) u_k(\mathbf{y}). \quad (3.29)$$

The adjoint field is found by solving the adjoint problem:

$$\hat{A}_{ik}^\dagger \tilde{u}_k = \varphi_i^*, \quad (3.30)$$

where the adjoint operator \hat{A}_{ik}^\dagger is defined through

$$\int_{\Omega} f(\mathbf{x}) (\hat{A}_{ik}(\mathbf{x}) g(\mathbf{x})) d\mathbf{x} = \int_{\Omega} (\hat{A}_{ik}^\dagger(\mathbf{x}) f(\mathbf{x})) g(\mathbf{x}) d\mathbf{x}. \quad (3.31)$$

To further simplify this expression, the dependence of \hat{A} on p must be specified. A linear dependence is proposed here, though extending the formula to more complicated dependences is rather easy. Taking $\rho(\mathbf{y}) = \rho^0 p(\mathbf{y})$ and $C_{ijkl}(\mathbf{y}) = C_{ijkl}^0 p(\mathbf{y})$ in the definition of \hat{A}_{ik} from equation (2.12) implies

$$\frac{\delta \hat{A}_{ik}(\mathbf{y})}{\delta p}(\mathbf{x}) = -\rho^0 \omega^2 \delta_{ik} \delta(\mathbf{x} - \mathbf{y}) - \partial_j (C_{ijkl}^0 \delta(\mathbf{x} - \mathbf{y}) \partial_l \cdot) \quad (3.32)$$

$$= -\rho^0 \omega^2 \delta_{ik} \delta(\mathbf{x} - \mathbf{y}) - 2C_{ijkl}^0 \delta(\mathbf{x} - \mathbf{y}) \partial_j \partial_l. \quad (3.33)$$

Plugging this back into the integral in equation (3.29) gives

$$\omega^2 \rho^0 \tilde{u}_i(\mathbf{x}) u_i(\mathbf{x}) + 2C_{ijkl}^0 \tilde{u}_i(\mathbf{x}) \partial_j \partial_l u_k(\mathbf{x}) \quad (3.34)$$

which is comparatively easily evaluated.

Summarizing: in order to compute the gradient $\delta f_{\text{obj}}/\delta p(\mathbf{x})$ we first run a normal simulation, i.e. solve equation (3.8), to obtain \mathbf{u} . Then we run an adjoint simulation, i.e. we solve equation (3.30), to obtain $\tilde{\mathbf{u}}$. Finally, we calculate $\delta A(\mathbf{y})/\delta p(\mathbf{x})$, which is given in equation (3.33) in the case of a linear material parameter dependence on p , and obtain the gradient through equation (3.29). This gradient tells us *at every point in the design* if p should be increased or decreased in order to increase f_{obj} . The next section will describe more precisely how this is used to optimize the design.

3.2 Optimization Algorithms

In this section I motivate why the gradient is so useful and how it will be used in my algorithm. I begin by describing the advantages of gradient based optimization algorithms over those that don't use the gradient. Following that I describe gradient descent, the most basic gradient based optimization method, as well as Adaptive Moment Estimation (ADAM), which is the algorithm that I have used.

An optimization algorithm is an algorithm for finding the optimum of a function. The function is often called the *objective function* or the *cost function*. A very naive optimization method would be to simply try some number of inputs and then choose the one with the highest function value. This requires a large number of points before a good value is found, meaning that it takes a long time. An improvement to this method is to use the information gained from the points already tried to decide which points to try next. If some point has a bad value, then try somewhere else; if some point has a good value, try another close by. Examples of algorithms that do this are bayesian optimization, particle swarm optimization, and various forms of genetic algorithms [6]. However, if the domain of the objective function is very high-dimensional, "close by" is a very large space. For such functions, it is essential to know in which direction the function increases. That is why gradient based optimization algorithms are so powerful; they enable us to quickly find the right direction to go in for best improvement.

3.2.1 Gradient Descent

The simplest gradient based optimization algorithm is called *gradient descent*.⁴ Like all of the algorithms I will describe it is an iterative algorithm, meaning that it generates a sequence of points that converges to an optimum, and the next point in the sequence is derived from the previous ones. In the case of gradient descent, the next point is gotten by

$$p_n = p_{n-1} + \eta g_{n-1} \quad (3.35)$$

where η is the so called *learning rate* and g_{n-1} is the gradient of the objective function at p_{n-1} . For ordinary gradient descent the learning rate would be fixed, and choosing

⁴The reason for calling it gradient descent, instead of gradient ascent is simply a convention. Any maximization problem can be made into a minimization problem by multiplying that objective function by -1 , so which formulation one chooses is arbitrary. However, the convention of talking about gradient descent is so strong that I will stick to that terminology, even though I am solving a maximization problem.

an appropriate value for this parameter is one of the problems of this method. If a too high value is chosen, then the steps taken will be too large and the optimum might be missed entirely. A too low value results in too small steps which will yield a slow convergence. Most gradient descent implementations nowadays use a so called learning schedule, which means that η is not constant during the optimization. This introduces the additional problem of choosing how fast and between which values it should change.

3.2.2 Adaptive Moment Estimation (ADAM)

The ADAM algorithm is an improved version of gradient descent. It has three main differences:

1. Each dimension has a separate learning rate.
2. The learning rate is automatically set from the previously seen gradients.
3. The evolution carries some momentum.

Figure 3.1 shows the difference in performance between ADAM and Gradient Descent (GD). With a slightly too large learning rate, the GD algorithm gets stuck in an oscillation and makes very little progress towards the minimum. If the learning rate is decreased, the oscillations disappear but the stepsize is now too small to make it all the way to the true minimum. Since the ADAM algorithm has some momentum, the motion along the valley gets compounded while the motion perpendicular gets damped which means that the oscillations are not as much of a problem. The adaptive learning rate also means that the algorithm doesn't get stuck prematurely due to the small gradient at the bottom of the valley. Admittedly, this objective function is specifically chosen to showcase the advantages of ADAM, but it has been shown to outperform GD in almost all cases [16].

Listing 1 shows a pseudocode implementation of the ADAM algorithm, which has four important hyperparameters. The first is α which controls the order of the step size. The next p will never be much further away than α in any dimension. β_1 and β_2 control how quickly the momentum decays. The algorithm basically keeps an exponentially decaying average of the previous gradients and previous squared gradients. The β :s set the decay rate for these averages. Finally, there is ϵ , which serves to make the algorithm more stable. If the average magnitude of the gradient becomes much smaller than ϵ , the algorithm will slow down.

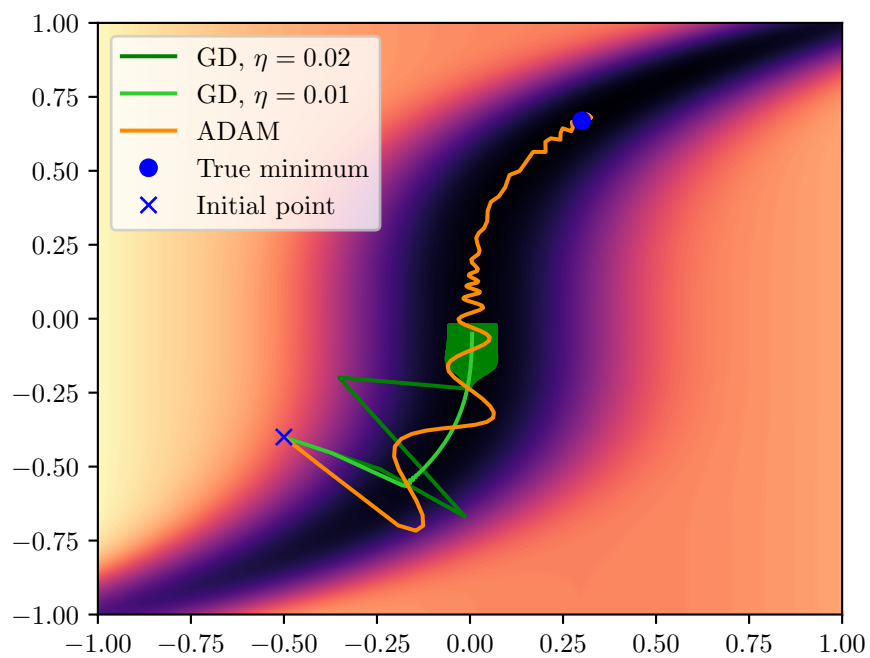


Figure 3.1: A comparison between ADAM and GD in an optimization landscape with a narrow canyon. The two different GD algorithms are shown with 1000 steps, while 200 steps with the ADAM algorithm are shown.

```
def adam(p_0, get_gradient, alpha,
         beta_1, beta_2, epsilon, n_iter):

    m = np.zeros(theta_0.shape)
    v = np.zeros(theta_0.shape)
    p = p_0

    for i in range(n_iter):
        g = get_gradient(theta)
        # Update biased first moment estimate
        m = beta_1 * m + (1-beta_1) * g
        # Update biased second moment estimate
        v = beta_2 * v + (1-beta_2) * g**2

        # Compute the bias-corrected estimates
        m_hat = m / (1 + beta_1**i)
        v_hat = v / (1 + beta_2**i)

        # Update p
        p += alpha * m_hat / (np.sqrt(v_hat) + epsilon)
```

Listing 1: Pseudocode for the ADAM algorithm. See [16] for a more in depth discussion of the algorithm.

3. Inverse Design

4. Methods

The aim of this thesis was to use inverse design to find a phononic beamsplitter. In this section I describe how that was accomplished. First I specify the skeleton of the device, i.e. the parts that were fixed, as well as the objective function. I then go on to specify how the simulations and optimization was done.

4.1 Design

The device design to be optimized can be seen in figure 4.1. The input and output waveguides consists of unit cells like the one in figure 2.1. The values for the parameters in the sketch are given in table 4.1. The reason for using this mode in this waveguide is that it has been shown to be interesting for avoiding mechanical leakage into the substrate on which it is clamped, as well as retaining a high optomechanical coupling [14].

Inside the design area, there can be one of two kinds of designs. The first is a *continuous design*, meaning that the material parameters ρ and C_{ijkl} are continuously varying. The range of values that they can take are between the density and elasticity of pure silicon and that of air. Any in-between values are obviously not something that can be physically realized, but it is useful as a first step in the optimization. This is parametrized through the *design field*, p , which takes values between 0, which means pure air, and 1, which means pure silicon. The second kind is a binary design, where each point either has silicon or not and there are no in-between values. This is accomplished using level-set methods, which will be explained in section 4.1.4.

Because the device is completely symmetric, only one half of it needs to be modeled, and the other half is extrapolated with a symmetry boundary condition.

4.1.1 Objective Function

The figure of merit of the device is how much of the input excitation gets transmitted into the output beams. Furthermore, all of the excitation of the output waveguide should be in the same mode that was excited at the input. Therefore, a mode overlap integral is used:

$$I = \int_{\Omega_1} \mathbf{u}(\mathbf{x}) \cdot \mathbf{u}_m^*(\mathbf{x}) d\mathbf{x}, \quad (4.1)$$

where \mathbf{u}_m is the shape of the mode (figure 2.3a). Because I am not interested in the phase of the output waves, the absolute value squared of the overlap integral is

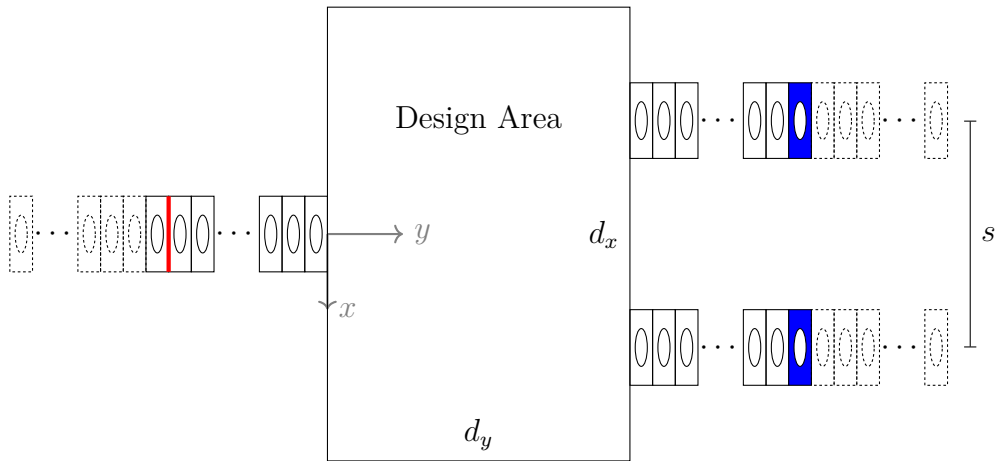


Figure 4.1: Device design to be optimized. At the red line, a wave traveling right is excited. The output is measured over the blue unit cells. The dashed unit cells are Perfectly Matched Layers (PMLs). The large, rectangular design area has dimensions $d_x \times d_y \times h$.

Table 4.1: Values for the geometric parameters of the device. Reference figures 2.1 and 4.1 for what the quantities mean.

Parameter	value
a	187 nm
w	187 nm
h_x	153.5 nm
h_y	49.5 nm
h	220 nm
d_x	$6w$
d_y	$4w$
s	$3w$

taken as the objective function,

$$f_{\text{obj}} = |I|^2 = II^*. \quad (4.2)$$

This will be maximal when the excitation of the mode m in the output waveguide is maximized, regardless of which phase it has.

The functional derivative of f_{obj} with respect to p then becomes

$$\frac{\delta f_{\text{obj}}}{\delta p}(x) = \frac{\delta I}{\delta p}(x)I^* + I\frac{\delta I^*}{\delta p}(x) \quad (4.3)$$

$$= \frac{\delta I}{\delta p}(x)I^* + \left(I^* \frac{\delta I}{\delta p}(x) \right)^* \quad (4.4)$$

$$= 2\text{Re} \left(\frac{\delta I}{\delta p}(x)I^* \right). \quad (4.5)$$

The derivative of I was derived in section 3.1.2.

4.1.2 Excitation

In order to excite the input waveguide in the desired mode, the stress on the boundary of a unit cell was exported from a unit cell eigenmode simulation with $k = 0.9\pi/a$ and applied to the boundary marked in red in figure 4.1. Since the frequency is perfectly controlled, this should excite only the desired mode, since that is the only permitted mode close by as seen in the band diagram in figure 2.2.

In order to confirm that the excitation was indeed fully in the desired mode, a separate model with only a waveguide with 200 unit cells was created. After applying the excitation and running the simulation, the proportion of the excitation that ended up in the desired mode was calculated. This was done by first calculating the mode overlap integral $\int \mathbf{u}\mathbf{u}_m^* d\mathbf{x}$ and comparing that to the norm of the displacement field $\int \mathbf{u}\mathbf{u}^* d\mathbf{x}$. If \mathbf{u} is written as $\mathbf{u} = a\mathbf{u}_m + b\mathbf{u}_r$ where a and b are scalars and \mathbf{u}_r is orthogonal to \mathbf{u}_m , then $\int \mathbf{u}\mathbf{u}^* d\mathbf{x} = a \int \mathbf{u}\mathbf{u}_m^* d\mathbf{x} + b \int \mathbf{u}\mathbf{u}_r^* d\mathbf{x}$. And since \mathbf{u}_r is orthogonal to \mathbf{u}_m , $a = \int \mathbf{u}\mathbf{u}_m^* d\mathbf{x} / \int \mathbf{u}_m\mathbf{u}_m^* d\mathbf{x}$, which enables us to calculate b as well. The result was near perfect ($b < 0.03a$) excitation of only the desired mode. Since energy is proportional to the square of the amplitude, $b < 0.03a$ means that $> 99.9\%$ of the energy was in the correct mode. To obtain such high fidelity, it was important that the mesh used for the unit cells in the wave guide was the same as the mesh in the unit cell simulation. High fidelity was also achieved if both meshes were made very fine, but such fine meshes carries a prohibitively large computational cost.

4.1.3 Perfectly Matched Layers (PMLs)

Ideally, the input and outputs are infinite waveguides. Unfortunately, simulating infinite waveguides would take infinite time. Instead, PMLs are placed at the caps of the input and output waveguides. The purpose of the PML is to absorb any

incoming waves without reflection, which would make it act as if there was an infinite waveguide on the other side into which the waves propagate indefinitely. One way to accomplish this is to add an imaginary component to the density of the material. The imaginary part must be introduced smoothly, otherwise the abrupt change in material parameters would induce reflections anyway. Therefore, the imaginary part is taken to be exponentially increasing, starting at y_0 and continuing until the end of the waveguide, n unit cells later. Furthermore, the curve is shifted vertically such that it is 0 at $y = y_0 - n$, and rescaled so that it is $\rho_{\text{si}} s$ at $y = y_0$.

$$\rho_{\text{im}} = \rho_{\text{si}} \cdot s \cdot \frac{e^{-|y-y_0|/d} - e^{-n/d}}{1 - e^{-n/d}} \quad (4.6)$$

Figure 4.2 shows the effect of changing these parameters on the shape of the profile of the imaginary component.

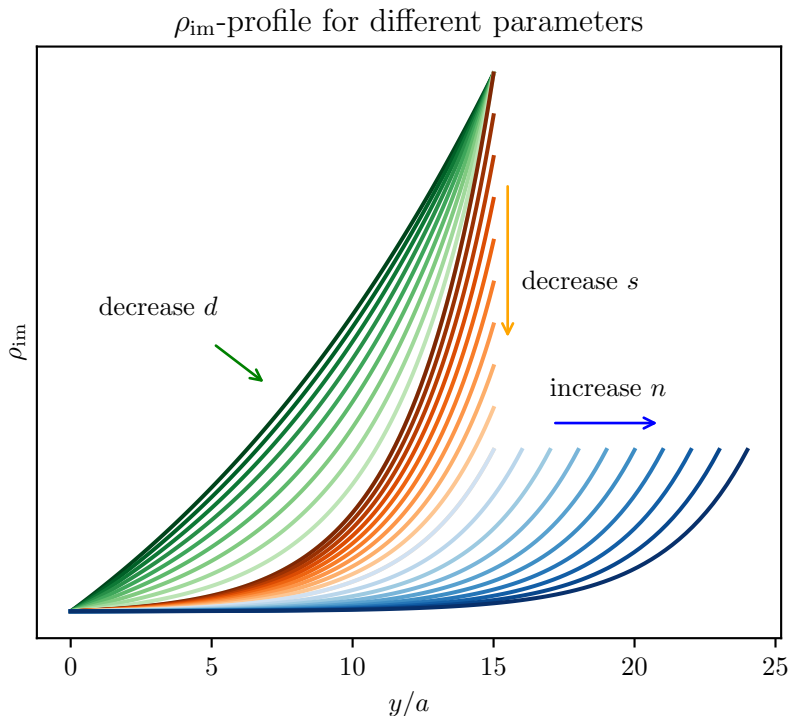


Figure 4.2: This figure shows the effect of changing different parameters. The green curves show changing d while keeping the other parameters fixed, and the orange and blue show s and n respectively. Darker colour means higher value, and the last green curve coincides with the first orange, and the last orange with the first blue.

There are three possible sources of reflections. Firstly, if the transition from no imaginary component to some imaginary component is too abrupt, that causes reflections. Secondly, if the imaginary component is too small, the waves will not be dampened completely when they reach the end of the PML and thus reflect off of that. And lastly, if d is small then there can be reflections from the steep increase

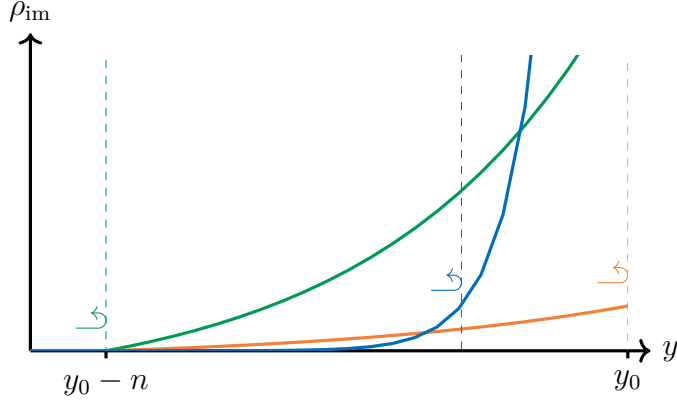


Figure 4.3: For the green curve, the initial sudden increase of the imaginary component of the density at the beginning of the PML causes reflections. For the blue curve, the beginning of the PML is smooth but there is an increase partway through sharp enough to cause reflections. For the orange curve, the PML never becomes strong enough to completely dampen the waves, and they get reflected at the end.

that happens some distance away from the beginning of the PML. See figure 2.2 for an illustration of where the different types of reflections occur.

It is desirable to make n as small as possible while still eliminating all reflections. In order to do so, a long waveguide with the same parameters as used for the input and output waveguides in the beamsplitter design was created. To discern where there was some component of the wave reflected, a fourier transform of the displacement field was made. The parameters controlling the shape of the ρ_{im} curve were then varied and an appropriate value was selected.

4.1.4 Level-Set

Ultimately, the device should consist of regions of material and regions of no material. There are basically two ways of doing this. The first, and perhaps most intuitive, is to simply store the coordinates of the boundary between the filled and empty regions. In addition to storing the coordinates, one must also store which points neighbour which. The second method, which is the one used in this report, is called the *level-set method*. In this method, the boundary is not directly stored, but rather is stored via an *implicit function*, $\phi(x)$, defined such that the boundary is the 0-isocontour of ϕ , i.e. the points x where $\phi(x) = 0$.

There are two main advantages of using the level-set method rather than directly storing the boundary points. Firstly, when moving the boundary we would like to do so in the normal direction, as moving it along itself has no effect. Computing the normal direction of a directly stored boundary is slightly cumbersome, though certainly achievable. With level-set, moving the boundary in the normal direction is as easy as adding a constant to the implicit function. Secondly, while the boundary is

4. Methods

changing, the resolution in one part might need to be increased while the resolution in another needs to be decreased. Deciding where and when to add new points is non-trivial when directly storing the boundary. Furthermore, if two boundaries merge, or if one splits in two, points need to be removed and the connectivities changed, which is quite complex. Figure 4.4 illustrates these problems with direct storage concretely. Both of these issues are automatically handled with the level-set method.

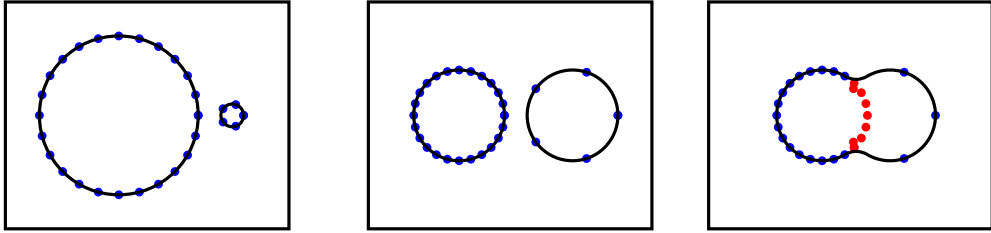


Figure 4.4: Possible evolution of boundary. In the leftmost figure, the boundary is defined by pretty much evenly spaced points. In the center figure the boundaries have moved and the spacing is no longer even, and the right circle is very poorly resolved. The rightmost figure shows the boundary after the two circles moved closer together. Now there are multiple points that need to be removed, marked in red, and the connectivity of the points that remain must be changed such that the two boundaries are merged.

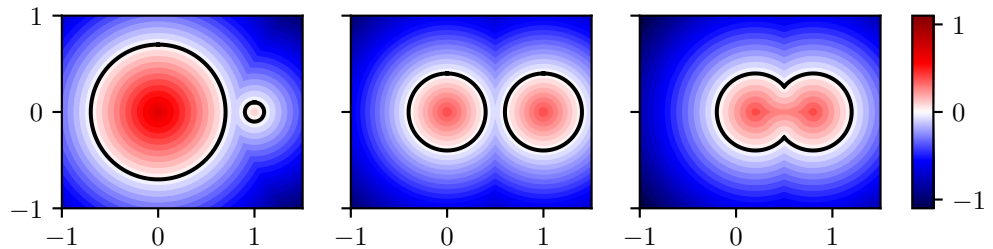


Figure 4.5: Example of three signed distance functions for three different boundaries.

There are of course a lot of possible functions $\phi(x)$ that have a given boundary as it's 0-isocontour. There is one choice that simplifies a lot of calculations though: the signed distance function. This function is defined as the distance from the closest point on the boundary, with a plus sign if it is inside and a minus sign if it is outside the boundary. See figure 4.5 for an example. It has the advantage that if one wishes to locally shift the boundary some length s in the normal direction, then simply add s to the function there. Figure 4.6 shows this effect in one dimension.

Using a signed distance function means that a gradient descent step can be taken by simply adding the gradient field to the signed distance field. However, there are some pitfalls that must be avoided. Firstly, the gradient needs to be rescaled so

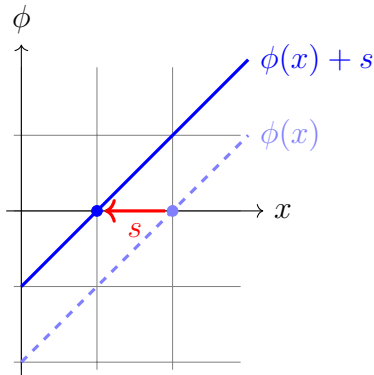


Figure 4.6: Adding s to the signed distance function shifts boundary by s .

that the boundary moves an appropriate distance. This has been done such that the boundary moves maximally 1 nm. Secondly, since the gradient is occasionally sharply peaked somewhere which may not lie near the boundary, only the gradient near the boundary is actually added to the signed distance field. After performing this addition, what was previously a signed distance field will now no longer be that, and thus the signed distance field is recalculated from the new boundary. This recalculation comes with a performance penalty, but since the COMSOL simulations are orders of magnitude slower than all other parts of the optimization, this is of little concern.

4.2 Optimization

For the optimization in the case of continuous optimization, the ADAM algorithm with one modification: a global learning rate was employed rather than individual learning rates. The reasoning for this was that individual learning rates would give jagged contours, which wouldn't be properly resolved by the meshing. Practically this modification means that `v` is a scalar and is set to `(1-beta_2)*np.mean(g**2) + beta_2 * v` in listing 1. The optimization was run and continually monitored, and once convergence was visually confirmed through looking at the plot of f_{obj} by iteration, it was terminated. A few different values for the β :s were tried, and in the end $\beta_1 = 0.9$ and $\beta_2 = 0.95$ were chose. However, it seemed that the evolution were not too sensitive to this choice. α was taken to be $2 \cdot 10^{-3}$, because that is large enough that p could change from 0 to 1 in 500 iterations, which was deemed an appropriate timescale since that took about one day.

The final step of the optimization was to use level-set for the design. However, just using the final device of the continuous optimization for the initial point of the level-set optimization would be a very large change, and there is no reason to expect that the resulting level-set design would be close to a design with good performance. Therefore, once the continuous optimization had converged, a sigmoid function was

applied to the design field p before ρ and C_{ijkl} were set:

$$\rho(\mathbf{x}) = \rho_{\text{si}}\sigma_r(p(\mathbf{x})), \quad C_{ijkl}(\mathbf{x}) = C_{ijkl}^{\text{si}}\sigma_r(p(\mathbf{x})), \quad \sigma_r(p) = \frac{1}{1 + e^{-(p-0.5)/r}}. \quad (4.7)$$

and then the optimization was restarted. This makes the design closer and closer to being binary, which means that the step to level-set designs aren't as significant and hopefully the initial design for the level-set optimization is not too far from a design with good performance.

Once that had been repeated a couple of times, the level-set design was initialized using the final design of the continuous optimization, and the level-set optimization was run.

4.3 Simulations

In this section I will detail some of the practicalities of performing the simulations. The simulation software used was COMSOL version 6.0. First, a unit cell with periodic boundary conditions was simulated. From that I obtain:

- the mode shape, used to calculate the component of the displacement field in the desired mode,
- the stress at the boundary, used as the force exciting the input waveguide,
- the frequency at which to excite in order to obtain a traveling wave with the desired wave vector.
- a mesh to be used when meshing the unit cells in the waveguides.

For the continuous optimization, the basic procedure went

1. Through the COMSOL-Matlab API, a beamsplitter model was made. The excitation force profile as well as the unit cell mesh and the mode shape was imported from the unit cell simulation.
2. A semi-random initial design field p was created. This was done by drawing a sample from a gaussian process, which means that the characteristic length scale that the design varies on could be controlled.
3. If the sigmoid function was to be used in this optimization, it was applied to the design field, and the result was saved to a different variable, that I call the interpolation field.
4. The interpolation field was imported to the COMSOL model, and the material parameters adjusted proportional to said field.

5. Both forward and backward simulations were run and the gradient was calculated and exported to Matlab.
6. With the gradient, the design field was updated and the algorithm returns to step 3.

For the level-set optimization, the procedure was basically the same, with some minor differences:

1. Through the COMSOL-Matlab API, a beamsplitter model was made. The excitation force profile as well as the unit cell mesh and the mode shape was imported from the unit cell simulation.
2. An initial signed distance field s was created. This was done by finding the $p = 0.5$ isocontour from the final iteration of the continuous optimization, and initializing a signed distance field from that.
3. The zero isocontour of the signed distance field was imported into the COMSOL model and a geometry was built from that.
4. Both forward and backward simulations were run and the gradient was calculated and exported to Matlab.
5. With the gradient, the signed distance field was updated and the algorithm returns to step 3. Note that as part of the update, the signed distance field was reinitialized so that it would not lose its properties.

4. Methods

5. Results and Discussion

In this chapter I present and discuss the results of my work. The first section, section 5.1, presents the simulations needed to ascertain that the beamsplitter simulations would work as intended. This includes tuning the PML parameters and checking that the excitation excites the right mode. After that, I present the results of the continuous optimization followed by the results for the level-set optimization in sections 5.2 and 5.3 respectively. In summary, the continuous optimization yielded near perfect devices with full transmission and very little reflection. The level-set optimizations never reached quite as good performance, reaching a 45/45 splitter with around 10% of the power getting reflected.

5.1 Long Waveguide Simulations

As detailed in chapter 4, a long waveguide without any beamsplitter elements was simulated to ascertain that the excitation method correctly excited only the desired mode, and that the PML elements were reflectionless. In this section I present the results from those simulations. The waveguide used for these is pictured in figure 5.1.



Figure 5.1: This figure shows the long waveguide used for the PML simulations as wells as validating the excitation method.

5.1.1 Excitation

The fact that the excitation was almost solely in the desired mode was verified in two ways. Firstly, as detailed in section 4.1.2, a and b in $u = au_m + bu_r$ was computed. The result was that $a = 1.166$ and $b = 0.0327$. Thus 99.92% of the energy was in the desired mode. Secondly, a fourier transform of the y-component of the displacement field was made. This can be seen in figure 5.2. The other modes that could be excited at this frequency have very different wave vectors, which means that they would show up as separate peaks somewhere around $0.4\pi/a$ and $0.1\pi/a$. Since no other peaks can be seen, this further supports the result that only the desired mode is excited.

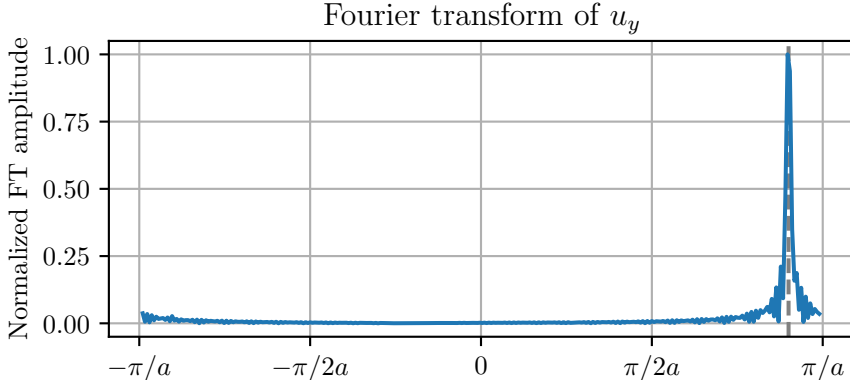


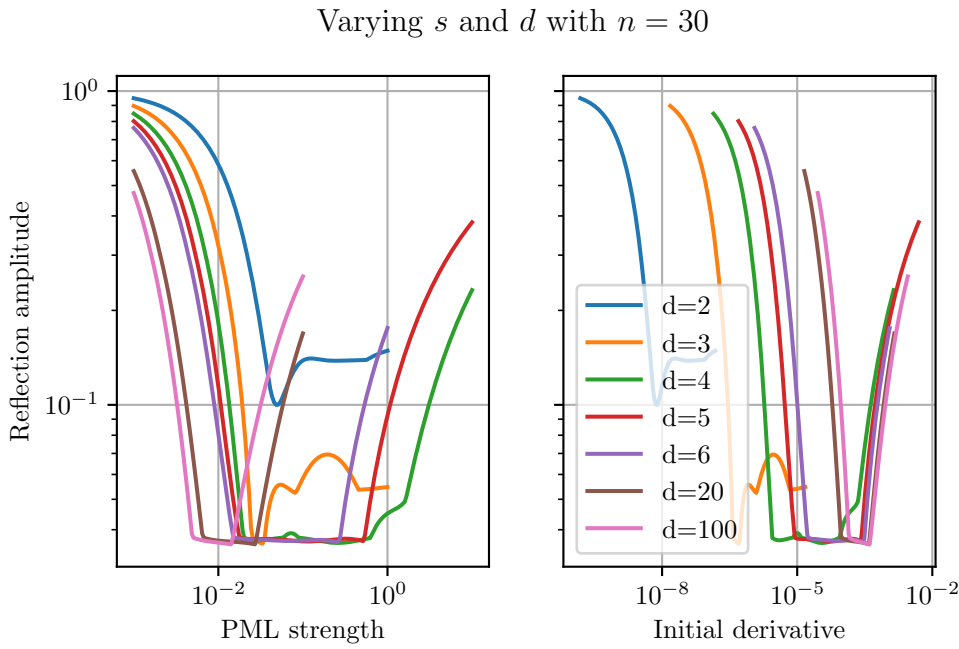
Figure 5.2: Fourier transform of the y -component of the displacement field. It clearly shows one wave traveling forward with a k -vector of $0.9\pi/a$, where the dashed gray line is. Since the closest other mode at this frequency is at $k_y \approx 0.4\pi/a$, where no peak is visible, it is concluded that solely the desired mode is excited.

5.1.2 PML Investigation

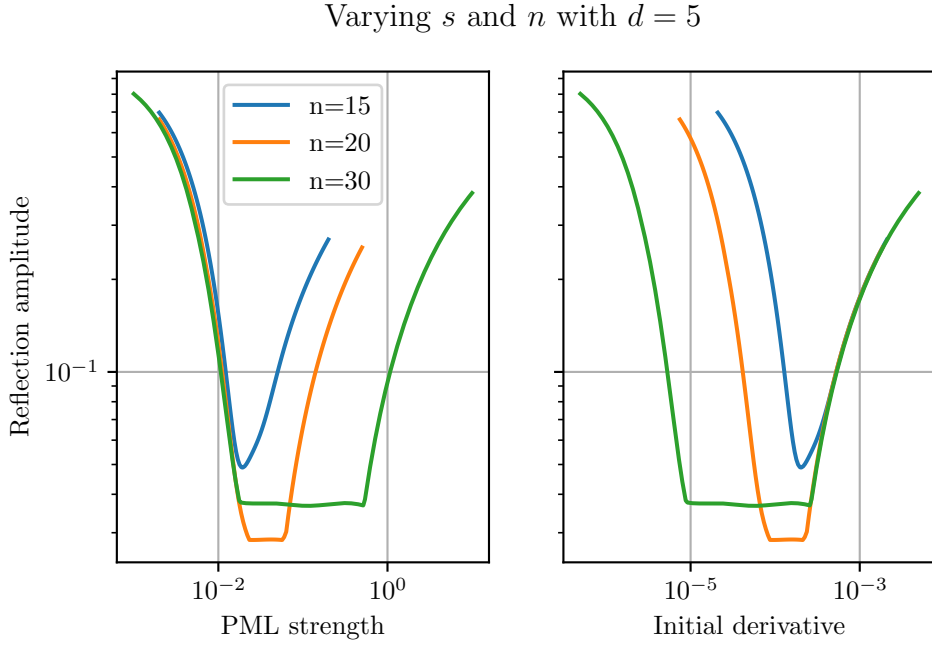
Figure 5.3 shows the amplitude of the reflection, quantified as the peak height relative to the forward propagating wave, for different profiles. These figures fit well with the three types of reflection mentioned previously. The leftmost plot in figure 5.3a shows that all of the different shapes yield reflections when the derivative at the beginning of the PML is around $3 \cdot 10^{-4}$, which indicates that the reflections are dominated by effects from the sudden start of the PML. On the other end, the increase in reflection amplitude come from waves reaching the end of the PML and getting reflected there. The third type of reflection seems to only be noticeable for $d \leq 4$. It is also worth noticing that with lower d , the plateau where neither of the first two kinds of reflections are significant is broader. Since $d = 5$ was the lowest d to show no signs of the third type of reflection, that was chosen for the shape of the PML profile. After that, I investigated how short I could make the it while retaining low reflections. Figure 5.3b shows s sweeps for different n . To achieve a short yet functional PML, $d = 5$, $s = 0.03$ and $n = 20$ was chosen. For $n = 15$, reflections from the beginning start to become significant before the reflections from the end have waned.

5.2 Continuous Optimization

There was a lot of problems with the optimization of the continuous design. Many optimization runs would end up looking like figure 5.4, reaching a somewhat performant beamsplitter but invariably declining after some point. The figure shows the evolution of the transmitted power in one of the output arms, as well as the reflected power back into the input. This has been normalized such that 1 is the power in through the input waveguide. Thus, an optimal beamsplitter would reach a transmission of 0.5. If the powers do not add up, it is because energy is flowing out in a different mode.



(a) On the left is the reflection amplitude plotted as a function of the PML strength s for different d . For $d > 4$ there are two sources of reflection: for small s reflection at the end of the PML occurs, and for large s , there is reflection at the beginning. The right figure makes it clear that it is the slope at the beginning of the PML that matters, since the point at which it becomes significant is the same for all d .



(b) This is the same as figure 5.3a but with varying n . For $n = 15$, the reflections from the beginning do not subside before the reflections from the end become significant, so at least $n = 20$ is necessary.

Figure 5.3

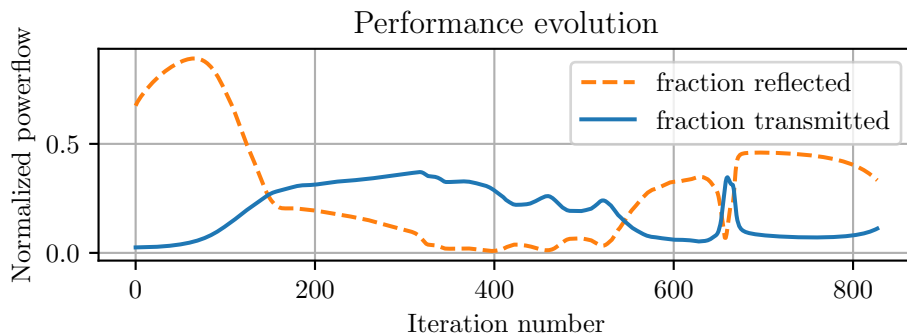


Figure 5.4: Non-converging optimization example. The blue curve shows the transmitted power in one of the output arms as a function of iteration, while the yellow shows the power reflected back out through the input. The cases where two times the blue plus the yellow isn't 1.0 is explained by power exiting through a different mode.

I tested a few different theories on why the algorithm might fail to converge. The first one was that perhaps the simulations were unstable for the case when $p \approx 0$. To test this I interpolated between ρ^{si} and 1000 kg/m^3 instead. However, convergence was still not reached. The second was that maybe the meshing was too coarse to resolve the design field properly. However, this was not the case as increasing the meshing did not change the objective function more than a percent or so. The last thing I thought of was that comsol was using quadratic shape functions for the fields. This means that on each finite element of the mesh, the fields are approximated with quadratic polynomials. Thus, if one computes any third order spatial derivative, it will be 0 everywhere, and the second order derivatives will not be very accurate. In figure 5.5 I show how quadratic splines can give a very good approximation to a function, while still being a terrible approximation to its second derivative. Since I used second derivatives in computing my gradient, that also wasn't very reliable. One way of solving this is to use higher order shape functions, however this greatly increases the degrees of freedom, making the problem too computationally expensive, at least with our hardware and geometry. Another way is to make the mesh much finer, but this is also too computationally expensive.

However, there was another way: using the built in COMSOL function `fsens` for computing the gradient, convergence was obtained. Figure 5.6 shows the performance evolution of this optimization run. At iteration 467, the model was deemed to have converged and as described in section 4.2, a sigmoid function with $r = 0.1$ was applied and optimization continued. At iteration 615, the model again seemed converged and r was set to 0.05. Finally, at iteration 830, near perfect performance was reached and optimization was terminated. Figure 5.7 shows the design field after convergence for each of the three stages.

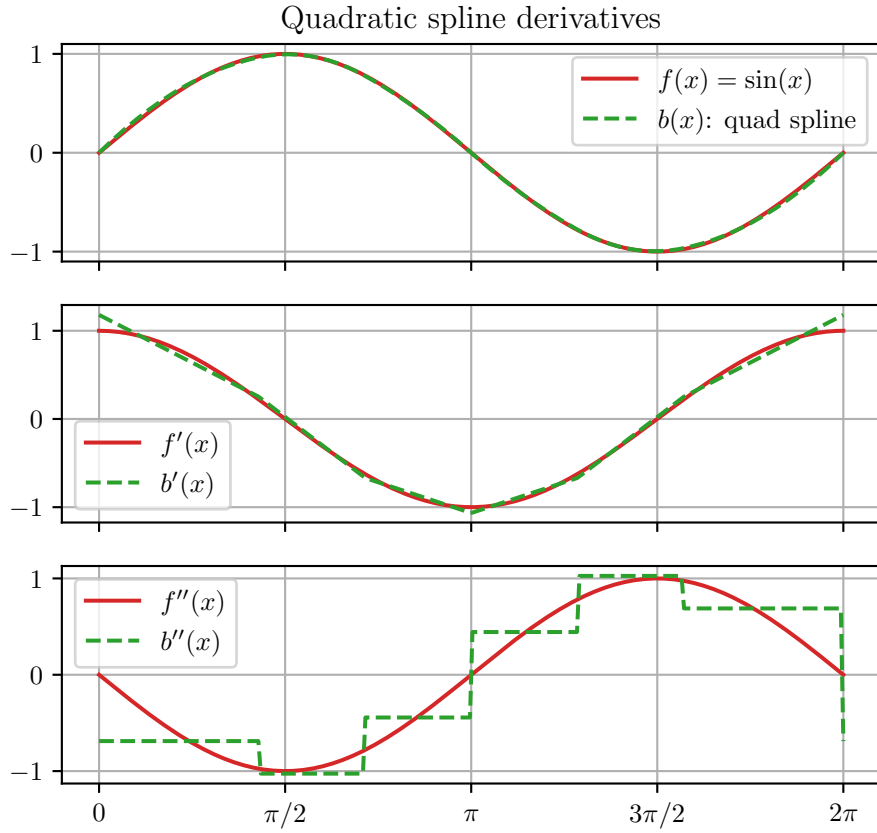


Figure 5.5: This figure shows a quadratic spline approximation to a sine function, given eight points on the function. Even though the spline approximates the sine function very well, the second derivative approximation is terrible.

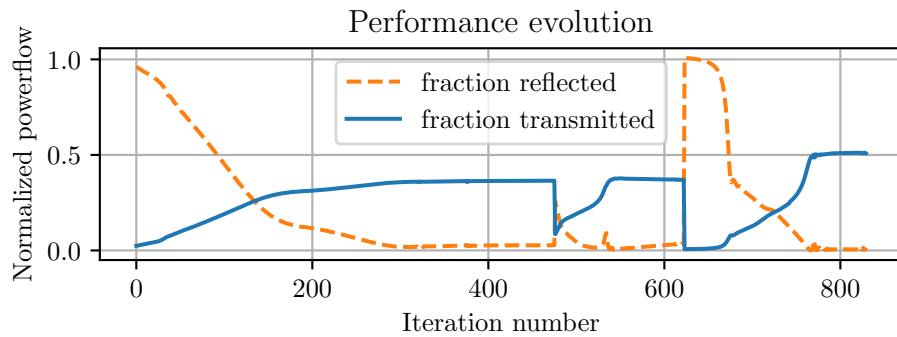


Figure 5.6: Similar to figure 5.4, but at iteration 467 and 615, a sigmoid function was abruptly applied to the design field, which causes the dips. The final device was a near perfect beamsplitter, with less than 1 % of the power begin reflected, and nothing being scattered into other modes.

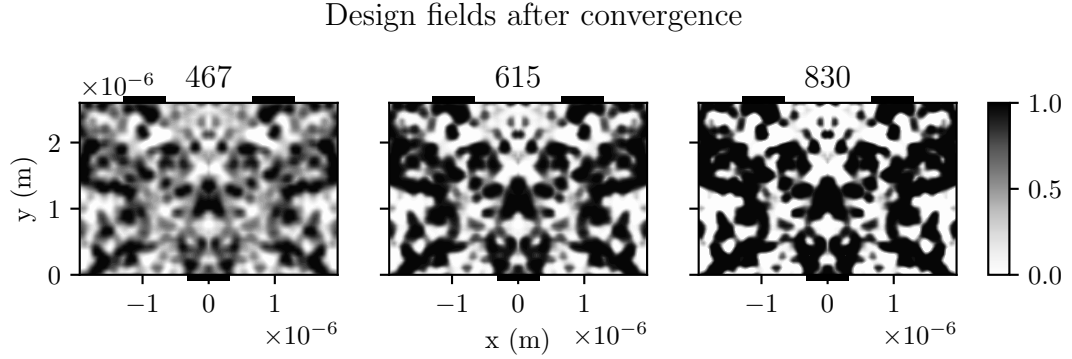


Figure 5.7: This figure shows the interpolation field at iteration 467, 615, and 830. It is clearly seen that the device becomes closer and closer to being binary.

5.3 Level-Set Optimization

The initial contour of the device was taken as the 0.5-isocontour of the final design field from the continuous optimization. Figure 5.8 shows the convergence plot for the level-set optimization, and figure 5.9 shows the final device. The performance did reach quite high values: splitting the input power roughly 45/45, though it never achieved the perfect 50/50 that was seen after the continuous optimization. Something to note is that the device does seem to be rather sensitive; a shift of only a nanometre can greatly change the device performance. Therefore the α chosen for the algorithm had to be set as low as 0.5 nm. Another important note is that the final design is rather close to the initial, so the starting point is very important for how high performance can be reached.

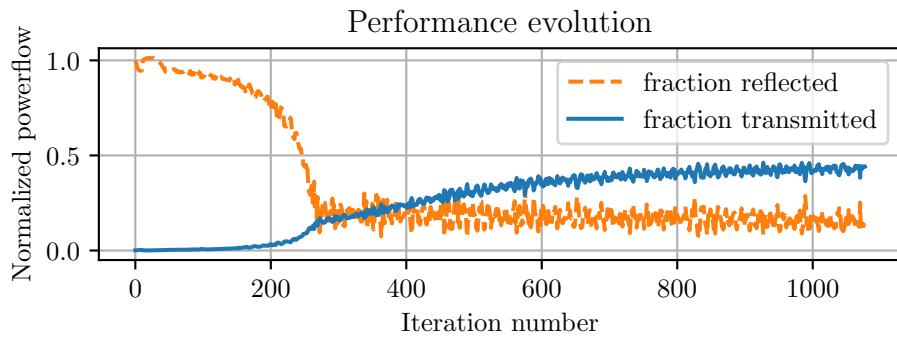


Figure 5.8: Performance evolution of the level-set device during optimization. The curve is not as smooth as the curve from the continuous optimization, which indicates that the step size is closer to being too large.

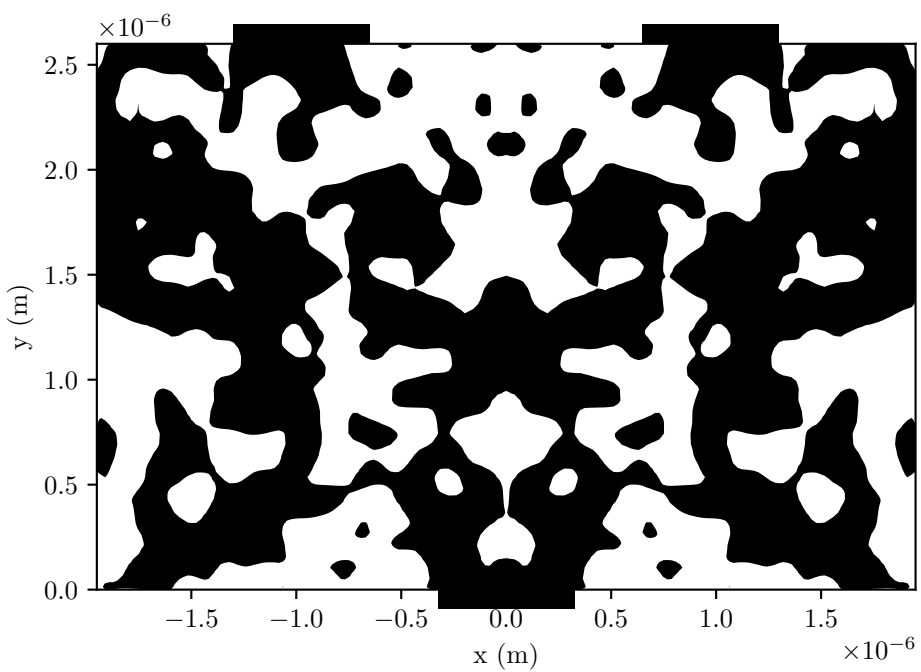


Figure 5.9: This figure shows the final optimized design for the level-set optimization. The device performs a roughly 45/45 split of the incoming power, with the rest of the power being reflected.

5. Results and Discussion

6. Concluding Remarks

Phononics have the potential to become a vital part of quantum information processing architecture, but devices are still limited to those that can be investigated through analytical means and/or be optimized with brute force methods. This study set out to investigate whether inverse design with adjoint simulation could be used to design so far unrealized devices and enable little explored applications.

I first examined theoretically the applicability of adjoint simulation on phononics, from which I concluded that the methods should work in theory. The second aim of this thesis was to demonstrate the utility of this method by designing a phononic beamsplitter. To do that, the process was split into two stages, a first where the material was allowed to vary continuously, and a second where a binary design was enforced using level-set methods. The continuous optimization yielded near perfect performance, validating the theoretical derivations. These results indicate that the inverse design concept can be very useful for designing phononic devices going forward. The level-set optimization never did achieve perfect performance, but decent performance was still reached. The author remains hopeful that the problems with the latter stage can be solved though, which would be a major step forward.

6.1 Future Research

There are a great number of potential paths that can be explored from this point, and the positive results presented here warrant further efforts in this area. One important improvement that should be investigated is the sensitivity of the device to small changes in the design. If it is very sensitive, imperfections in fabrication could be detrimental to the devices performance. There may be some ways of mitigating this however, for example by running multiple simulations with small perturbations in the design and averaging them to obtain the objective function. Another potential path of exploration is the limiting of the feature size. This could also be done by augmenting the objective function, but this time with a pure part that punishes small features.

In addition to method improvements, another path is to apply this to designing other types of devices. For example, waveguide bends seem to be well suited for this type of design, and would be useful if one wishes to use phononic waveguides for routing excitations around on a chip. It may also be possible to inverse design hybrid devices that use both optics and mechanics for example, though that would likely require a significant effort.

6. Concluding Remarks

References

- [1] P. Arrangoiz-Arriola, E. A. Wollack, Z. Wang, *et al.*, “Resolving the energy levels of a nanomechanical oscillator,” *Nature*, vol. 571, no. 7766, pp. 537–540, Jul. 2019, Number: 7766 Publisher: Nature Publishing Group. DOI: 10.1038/s41586-019-1386-x. [Online]. Available: <https://www.nature.com/articles/s41586-019-1386-x> (visited on 2023-04-14).
- [2] E. A. Sete and H. Eleuch, “High-efficiency quantum state transfer and quantum memory using a mechanical oscillator,” *Physical Review A*, vol. 91, no. 3, p. 032309, Mar. 17, 2015, Publisher: American Physical Society. DOI: 10.1103/PhysRevA.91.032309. [Online]. Available: <https://link.aps.org/doi/10.1103/PhysRevA.91.032309> (visited on 2023-06-02).
- [3] G. S. MacCabe, H. Ren, J. Luo, *et al.*, “Phononic bandgap nano-acoustic cavity with ultralong phonon lifetime,” *Science*, vol. 370, no. 6518, pp. 840–843, Nov. 13, 2020. DOI: 10.1126/science.abc7312. arXiv: 1901.04129 [cond-mat, physics:quant-ph]. [Online]. Available: <http://arxiv.org/abs/1901.04129> (visited on 2023-06-06).
- [4] A. H. Safavi-Naeini, D. V. Thourhout, R. Baets, and R. V. Laer, “Controlling phonons and photons at the wavelength scale: Integrated photonics meets integrated phononics,” *Optica*, vol. 6, no. 2, pp. 213–232, Feb. 20, 2019, Publisher: Optica Publishing Group. DOI: 10.1364/OPTICA.6.000213. [Online]. Available: <https://opg.optica.org/optica/abstract.cfm?uri=optica-6-2-213> (visited on 2023-04-19).
- [5] H. Qiao, E. Dumur, G. Andersson, *et al.*, *Developing a platform for linear mechanical quantum computing*, 2023. arXiv: 2302.07791 [quant-ph].
- [6] P.-I. Schneider, X. Garcia Santiago, V. Soltwisch, M. Hammerschmidt, S. Burger, and C. Rockstuhl, “Benchmarking five global optimization approaches for nano-optical shape optimization and parameter reconstruction,” *ACS Photonics*, vol. 6, no. 11, pp. 2726–2733, 2019.
- [7] Y. Zhang, S. Yang, A. E.-J. Lim, *et al.*, “A compact and low loss y-junction for submicron silicon waveguide,” *Optics Express*, vol. 21, no. 1, pp. 1310–1316, Jan. 14, 2013, Publisher: Optica Publishing Group. DOI: 10.1364/OE.21.001310. [Online]. Available: <https://opg.optica.org/oe/abstract.cfm?uri=oe-21-1-1310> (visited on 2023-04-19).
- [8] S. Molesky, Z. Lin, A. Y. Piggott, W. Jin, J. Vucković, and A. W. Rodriguez, “Inverse design in nanophotonics,” *Nature Photonics*, vol. 12, no. 11, pp. 659–670, Nov. 2018, Number: 11 Publisher: Nature Publishing Group. DOI: 10.1038/s41566-018-0246-9. [Online]. Available: <https://www.nature.com/articles/s41566-018-0246-9> (visited on 2023-04-14).

- [9] L. Su, D. Vercruyse, J. Skarda, N. V. Sapra, J. A. Petykiewicz, and J. Vuckovic, “Nanophotonic inverse design with spins: Software architecture and practical considerations,” 2019. arXiv: 1910.04829 [physics.app-ph].
- [10] J. S. Jensen and O. Sigmund, “Systematic design of photonic crystal structures using topology optimization: Low-loss waveguide bends,” *Applied Physics Letters*, vol. 84, no. 12, pp. 2022–2024, Mar. 16, 2004. DOI: 10.1063/1.1688450. [Online]. Available: <https://doi.org/10.1063/1.1688450> (visited on 2023-05-28).
- [11] A. Y. Piggott, J. Lu, T. M. Babinec, K. G. Lagoudakis, J. Petykiewicz, and J. Vučković, “Inverse design and implementation of a wavelength demultiplexing grating coupler,” *Scientific Reports*, vol. 4, no. 1, p. 7210, Nov. 27, 2014. DOI: 10.1038/srep07210. arXiv: 1406.6185 [physics]. [Online]. Available: <http://arxiv.org/abs/1406.6185> (visited on 2023-05-28).
- [12] S. Han, Q. Han, and C. Li, “Deep-learning-based inverse design of phononic crystals for anticipated wave attenuation,” *Journal of Applied Physics*, vol. 132, no. 15, p. 154901, Oct. 19, 2022. DOI: 10.1063/5.0111182. [Online]. Available: <https://doi.org/10.1063/5.0111182> (visited on 2023-05-30).
- [13] J. Joannopoulos, S. Johnson, J. Winn, and R. Meade, *Photonic Crystals: Molding the Flow of Light 2nd edn Princeton Univ.* Princeton University Press, 2008.
- [14] J. Kolvik, P. Burger, J. Frey, and R. Van Laer, *Clamped and sideband-resolved silicon optomechanical crystals*, Mar. 31, 2023. DOI: 10.48550/arXiv.2303.18091. arXiv: 2303.18091 [physics, physics:quant-ph]. [Online]. Available: <http://arxiv.org/abs/2303.18091> (visited on 2023-04-14).
- [15] M. B. Giles and N. A. Pierce, “An introduction to the adjoint approach to design,” *Flow, Turbulence and Combustion*, vol. 65, no. 3, pp. 393–415, Dec. 1, 2000. DOI: 10.1023/A:1011430410075. [Online]. Available: <https://doi.org/10.1023/A:1011430410075> (visited on 2023-05-27).
- [16] D. P. Kingma and J. Ba, “Adam: A method for stochastic optimization,” 2017. arXiv: 1412.6980 [cs.LG].

DEPARTMENT OF MICROTECHNOLOGY AND NANOSCIENCE

CHALMERS UNIVERSITY OF TECHNOLOGY

Gothenburg, Sweden

www.chalmers.se



CHALMERS
UNIVERSITY OF TECHNOLOGY